Giblin, Stephen; Mykkanen, Emma; Kemppinen, Antti; Immonen, Pekka; Manninen, Antti; Jenei, Mate; Mottonen, Mikko; Yamahata, Gento; Fujiwara, Akira; Kataoka, Masaya

Realisation of a quantum current standard at liquid helium temperature with sub-ppm reproducibility

Published in:
Metrologia

DOI:
10.1088/1681-7575/ab72e0

Published: 01/04/2020

Document Version
Peer reviewed version

Realisation of a quantum current standard at liquid helium temperature with sub-ppm reproducibility: Supplementary Information

Stephen P. Giblin,[1] Emma Mykkänen,[2] Antti Kemppinen,[2] Pekka Immonen,[2] Antti Manninen,[2] Máté Jenei,[3] Mikko Möttönen,[3] Gento Yamahata,[4] Akira Fujiwara,[4] and Masaya Kataoka[1]

[1)] *National Physical Laboratory, Hampton Road, Teddington, Middlesex TW11 0LW, United Kingdom*

[2)] *VTT Technical Research Centre of Finland Ltd, National Metrology Institute VTT MIKES, Espoo, FI-02044 VTT, Finland*

[3)] *QCD Labs, QTF Centre of Excellence, Department of Applied Physics, Aalto University, PO Box 13500, FI-00076 AALTO, Finland*

[4)] *NTT Basic Research Laboratories, NTT Corporation, 3-1 Morinosato Wakamiya, Atsugi, Kanagawa 243-0198, Japan*

(Dated: 25 February 2020)

A. RAW DATA AND NOISE

Long integration times are required to resolve small currents to high resolution, making it important to account for the different sources of noise in the experiment. In figure S1(a), we show the Allan deviation of the current with the pump tuned to the $N = 1$ plateau and turned on, at both NPL and MIKES. We compare these to the Allan deviation expected for the Johnson current noise in the ULCA input. This noise is expected to be the largest single contribution to the total noise. It has a spectral density per unit bandwidth of $\sqrt{4k_{\mathrm{B}}T/R}$, with $R = 3$ GΩ: approximately 2.3 fA/$\sqrt{\mathrm{Hz}}$. The experimental Allan deviation is marginally above the ULCA noise floor due to small additional contributions such as the ULCA output noise and additional noise due to vibrations in the wiring of the cryogenic probe. The excellent stability of the ULCA[1] is clear, particularly from the MIKES data trace where there is no clear transition to a regime of $1/f$ noise for averaging times as long as 1000 s. This stability permits a long timescale for the on-off cycle of the pump measurement, a key advantage in the presence of unexpected time constants as discussed in section D below.

In figures S1(b-d) we show sections of raw time-domain data from high-precision pump measurements in which the AC drive to the pump was turned on and off. The presented data are segments of the data sets from runs NPL 1, MIKES 1 and Aalto presented in figure 4 of the main text. The only quantitative difference visible by eye is a slight change in the offset in the 'pump off' state between the NPL and MIKES systems. The differences in the ULCA gain and voltmeter calibration factors between the NPL and MIKES setups change the indicated on-off voltage difference by ~ 40 ppm, or around 7 μV.

B. ULCA STABILITY

In previous high-precision measurements of electron pump currents, the stability of the measuring system, whether based on a 1 GΩ standard resistor[2] or an ULCA[3], has become an important contribution to the overall uncertainty. In this work, an ULCA was used to convert the pump current to a voltage for subsequent readout by a precision-calibrated DVM. In figure S2, we present the calibration data for the two ULCA units employed: the NPL ULCA at NPL, and the MIKES ULCA at MIKES and Aalto. The time intervals for the high-precision electron pump measurements reported in the paper are indicated by vertical grey bands on both plots. Both ULCAs demonstrate a gain stability consistent with a published study, in which several ULCA units demonstrated a drift in the overall transresistance gain less than 1 ppm per year[4]. The change in the ULCA gain from one calibration to the next justifies a drift uncertainty term (see table 1 of the main text) of less than 0.1 ppm. This drift uncertainty was evaluated using the rectangular distribution in the same way as the drift uncertainty of the DVM calibration factor detailed in the next section, and in the supplementary information for Ref. 2

C. NPL HIGH-PRECISION MEASUREMENT SETUP

In all the reported high-precision measurements, the ULCA output was recorded by a precision digital voltmeter (DVM), the Keysight 3458A. The DVM is calibrated to yield the calibration factor C defined as the true voltage divided by the indicated voltage. Exceptionally stable examples of this model of DVM have demonstrated stability of the calibration factor as good as a few parts in 10^8 per day[5]. However, our experience in this study, and with previous studies at NPL[2,6,7] is that the C could change by up to a few parts in 10^7 per day. Even with daily calibrations directly against a Josephson array, as in the MIKES measurements, the use of a rectangular distribution yields a typical relative uncertainty due to drift of around 10^{-7}. To lower this uncertainty contribution, at NPL the DVM calibration interval was reduced to an hour by incorporating a switch (using one channel of a Data Proof DP320 scanner) into the measurement system as shown in figure S3(a). This switch allowed voltmeter calibrations to be interleaved with pump mea-

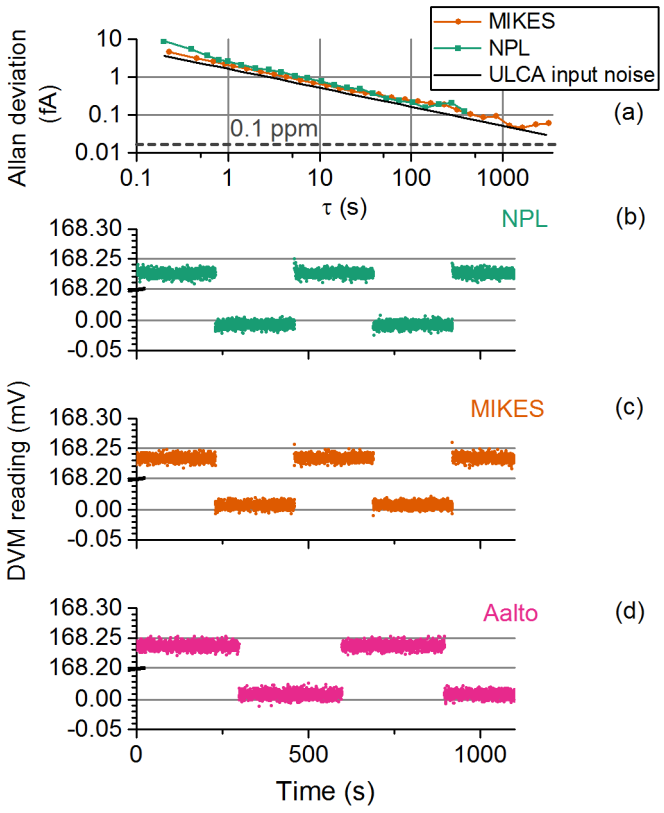

FIG. S1. (a): Filled symbols: Allan deviation computed from time-domain data traces at NPL and MIKES, in which the pump was continuously on. Solid line: theoretical Allan deviation for the Johnson current noise due to the ULCA input resistance. Horizontal dashed line: current corresponding to a part in 10^7 of $I_P \sim 168$ pA. (b)-(d): Raw DVM data, recording the ULCA output for precision measurements at NPL, MIKES and Aalto. In these measurements, the on-off cycle is effected by turning the RF pump signal on and off.

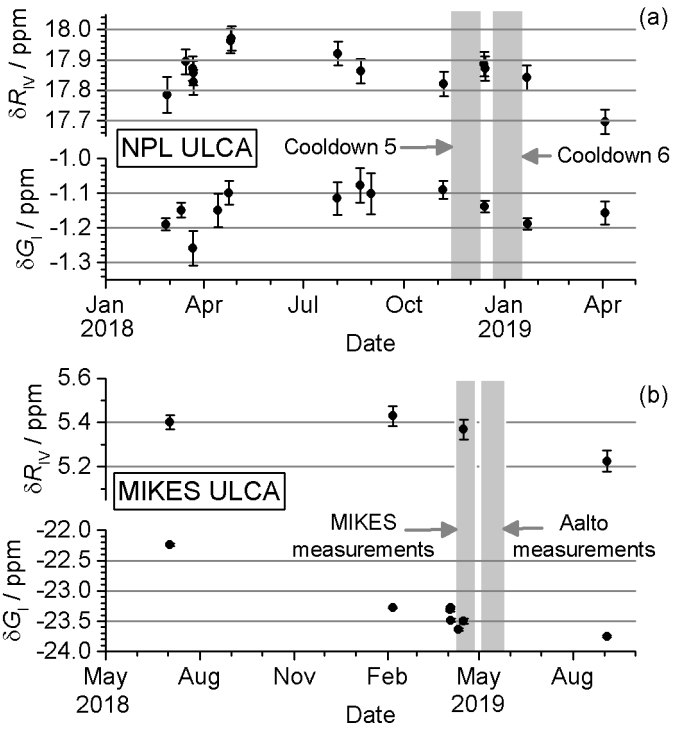

FIG. S2. Deviations from the nominal value of the output transresistance gain R_{IV} and of the input current gain G_I for (a) the NPL ULCA and (b) the MIKES ULCA. The time-spans of high-precision electron pump measurement campaigns are indicated by vertical grey bars.

surements, enabling a dramatic reduction in the uncertainty due to the voltmeter calibration. Figure S3(b) shows a section of raw DVM data from measurement NPL 1. On the left-hand side of the plot for elapsed run-time less than 22000 s, the input of the DVM is connected to the pump, and an on-off cycle is visible with 1000 data points for each on and off segment. The on-off difference signal ΔV is indicated on the plot. Then the switch connects the DVM to the Josephson array and 10 on-off cycles are executed with 100 data points per segment. A shorter cycle is possible during the calibration step, because the time constant is negligible. Because the Josephson array is a hysteretic type operating at zero current bias, the same voltage step is not obtained each time the array voltage is changed. However, this is not important since we are only interested in the gain factor of the DVM, not the offset. The array voltage is given by $V_J = nf/K_{J\text{-}90}$, with the step numbers n indicated on the plot and $f_J = 76.674$ GHz. Note that the calibration voltage and the ULCA output during a pump measurement are roughly equal, ~ 168 mV, and hence there is no need to correct for or add uncertainties due to the DVM non-linearity. The uncertainty in the DVM calibration factor from 10 calibration on-off cycles is typically in the range from 3×10^{-8} to 5×10^{-8}. The drift over the 1-hour calibration interval is also typically less than 5×10^{-8} although interestingly, larger jumps are occasionally observed with the largest jumps being a few parts in 10^{-7}, similar to the typical jumps in a 24 hour calibration interval. Each set of 10 pump measurement cycles is analyzed using the mean of the DVM calibration factors before and after the set, and the uncertainty in the DVM calibration is added to the statistical uncertainty of the pump measurement. The precision measurement run 'NPL 1' consists of 16 sets of 10 pump cycles each, interleaved with sets of 10 DVM calibration cycles, and lasts 22 hours.

Next we discuss the process of analysing the interleaved data in more detail, with reference to figure S3 (c) and (d). In figure S3 (c), we show as open circles the DVM calibration factors from run NPL 2. The error bars are the combination of type A and type B uncertainties in the DVM calibration, and are dominated by the type A contribution. Each sequence of pump measurement cycles is analyzed using the mean of the DVM calibration factors before and after the sequence:

$C_i = (C_{\rm before} + C_{\rm after})/2$. These mean values are shown as filled circles in figure S3 (c). The uncertainty in the mean values (shown as the error bars on the plot) is the root-sum-square of three contributions: the uncertainties in the two calibrations before and after the sequence, and a drift uncertainty which is taken from the rectangular distribution as $U_{\rm drift} = |C_{\rm before} - C_{\rm after}|/(2\sqrt{3})$. In the analysis of the pump measurement sequence, we extract the difference signal ΔV, and the pump current in the i'th sequence is evaluated as $I_{{\rm P}i} = C_i \Delta V / A_{\rm TR}$, where $A_{\rm TR}$ is the trans-resistance gain of the UCLA[1]. The values of $\Delta I_{{\rm P}i}$ are shown in figure S3 (d). The error bars are the root-sum-square combination of the type A uncertainty in ΔV, the uncertainty in C_i and the uncertainty in $A_{\rm TR}$. The weighted mean of the 13 values of $\Delta I_{\rm Pi}$ yields a normalised deviation of the pump current from $e_{90} f$ of $0.464 \pm 0.14 \times 10^{-6}$. Because this data was obtained by the gate switching method, a leakage current correction is applied to obtain the value of $\Delta I_{\rm P}$ shown in figure 4 of the main text.

An logical improvement to the setup would be to use the Josephson array voltage continuously as a voltage reference, so that the DVM measured a small difference between the ULCA output and $V_{\rm J}$. This 'null-voltage' approach was used in Ref. 3 and reduced the uncertainty due to the voltage calibration to a negligible level. In fact, it was attempted in the present study at NPL, but the JVS operation proved unreliable. This was probably due to the fact that the JVS was in a separate laboratory to the electron pump, and the two were connected by a $\sim$ 30-m-long cable. This cable did not add any significant noise when it was connected to the high-impedance input of the DVM, but the null-voltage circuit inevitably requires the low-voltage sides of the pump experiment and the JVS to be connected. It is likely that in this configuration, circulating ground currents caused an unacceptable amount of current noise through the Josephson junctions and prevented stable operation of the JVS.

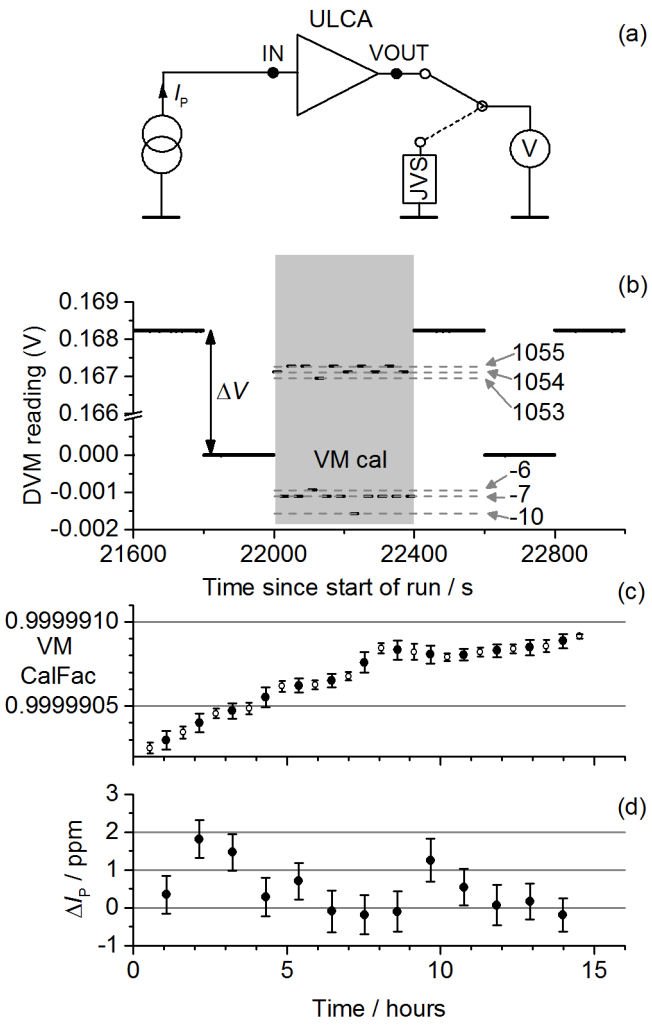

FIG. S3. (a): Schematic diagram of the NPL high-precision measurement circuit. JVS = Josephson Voltage Standard. (b): Section of raw voltmeter data taken from run NPL 1. The Josephson voltage step numbers during the DVM calibration cycles are indicated on the plot. A vertical arrow shows the difference voltage ΔV extracted from the pump measurement cycle. (c): DVM calibration factors measured during run NPL 2. Open circles: Measured DVM calibration factor. Filled circles: average of the adjacent calibration factors used for analysing each sequence of pump measurement. (d): Pump current evaluated from the 13 pump measurement sequences of run NPL 2. Plots (c) and (d) share the same x-axis.

D. TIME CONSTANTS

When the RF drive signal is turned on or off, the pump current settles with a time constant which has been a few seconds in all previous precision studies at NPL[2,6–9] and PTB[3,5]. In the present study, substantially longer time constants were observed. This required a correspondingly longer portion of the data to be rejected before analysis, and longer on-off cycles were used. Fortunately, the stability of the ULCA permitted on-off cycle times of several hundred seconds without $1/f$ noise compromising the type A uncertainty. In this supplementary section, we present data illustrating the time constants, and we discuss their possible origin.

Figure S4 shows temporal point-by-point averages of a number of representative raw sets of data. In this type of averaging, the first data point (plotted at zero time) is the average of the first data points of all the 'on' cycles (top panels) and all the 'off' cycles (bottom panels). The second data point is the average of all the second data points, and so on. In panels (a), (b), and (c), we show the point-by-point averages of data measured at NPL, Aalto and MIKES in which the RF pump signal was turned on and off. For comparison, in panel (a) we have included data from Ref. 6: there is clearly a time constant in the 4 K measurements which was not present in the 1.5 K measurements on the same sample. Different cryo-

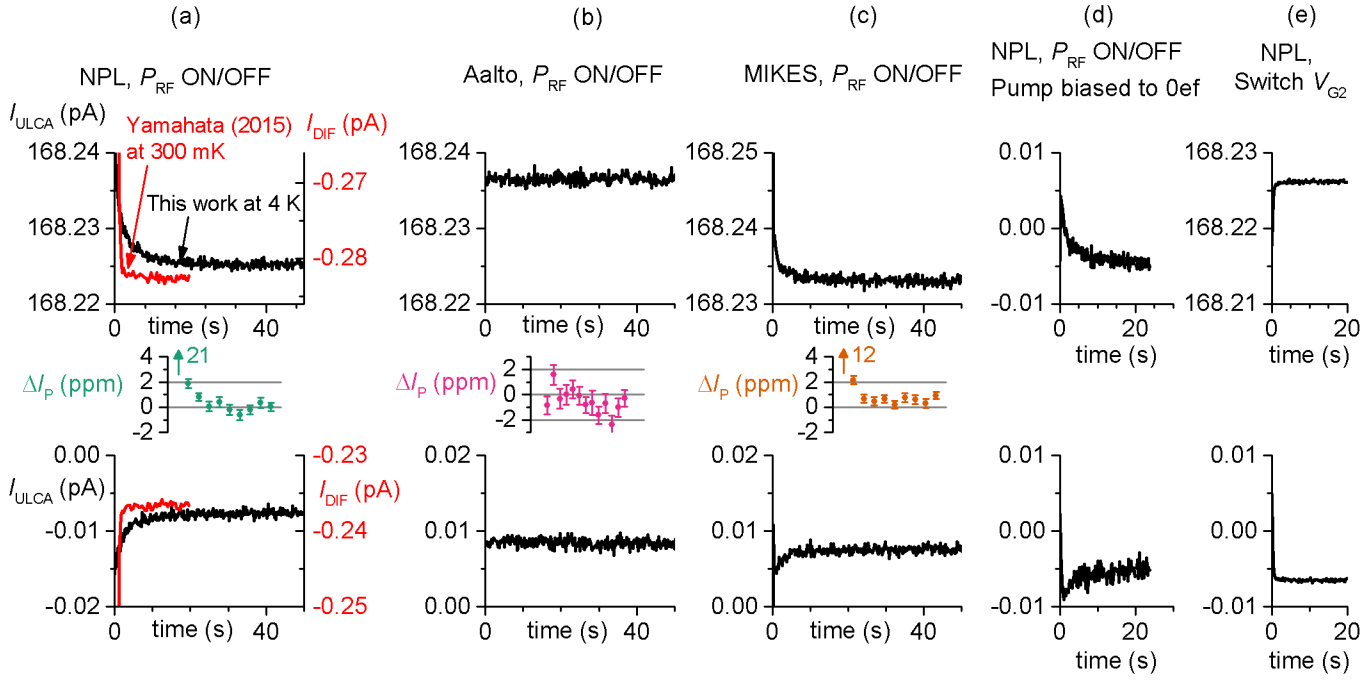

FIG. S4. Each main panel shows a point-by-point average (described in the text) of raw on-off data, with the y-axis of all plots covering the same range, 20 fA. The top panels show the averages in the on state, and the bottom panels show the averages in the off state. (a): NPL measurements from this study using the power switching method (black line, left y-axis), and data from Ref. 6 for comparison (Red line, right y-axis). The measurements of Ref. 6 were obtained using a different measurement system in which the raw current signal $I_{\rm DIF}$ is the difference between the pump current and a reference current. (b): Aalto measurements using the power switching method. (c): MIKES measurements using the power switching method. (d): NPL measurement using the power switching method in which the pump was biased to the $N = 0$ plateau. (e): NPL measurements using the gate switching method. The lower apparent noise in this data is because a shorter cycle was used for the gate switching on-off method (100 points instead of 1000 points per segment) and hence the point-by-point average is over a larger number of cycles than for the power switching method. The smaller inset panels in between the top and bottom main panels of (a), (b) and (c) show a 100-point moving-window analysis (described in the text) of the NPL, Aalto and MIKES precision measurements respectively, with vertical arrows indicating data points off the scale of the plot.

genic probes were used in the two measurements, and the sample was thermalised differently. In the experiments of Ref. 6, the sample was in vacuum and thermalised through the leads. In the present work, it was either immersed in liquid helium, or just above the liquid surface in helium vapour. The time constant is equal with the sample in liquid or vapour. The time constant observed in the NPL measurements is also present at MIKES but is completely absent in the Aalto data. For a different view of the time constant, the small inset panels show moving-window analyses of the precision measurements at NPL, MIKES and Aalto. In this analysis, $\Delta I_{\rm P}$ is calculated from a window of 100 data points in each data segment, offset from the start of the segment by a multiple of 100 points. The first data point along the x-axis in each inset plot is calculated from points 1 to 100 in each raw data segment, the second data point from points 101 to 200, and so on up to the last point which is calculated from points 1201 to 1300 for the Aalto data, and points 901 to 1000 for the NPL and MIKES data. The time constants in the NPL and MIKES measurements, and the absence of a time constant in the Aalto measurement, are also visible in this analysis. The ~ 0.5 ppm offset in the pump current in the MIKES measurements is clearly resolved, even with this analysis which rejects 90% of the data.

Figure S4(d) shows a point-by-point average from a test measurement in which the RF power is turned on and off, but with the pump biased off the plateau with $V_{\rm EXIT} = -1.7$ V, so that $I_{\rm P} = 0$. Turning the RF power on and off yields a transient current with a time constant very similar to that of the pumping data. The size of this transient is strongly dependent on $P_{\rm RF}$, and disappears for $P_{\rm RF} < 8$ dBm. This suggests that the transient current is due to heating caused by the dissipation of RF power in the vicinity of the sample. Figure S4(e) shows data for the gate switching cycle, in which the RF drive was on all the time, $V_{\rm EXIT}$ was switched from its operat-

ing point to a more negative value to turn the pump off. Here, the time constant is much shorter.

We briefly speculate on the origin of the time constant using the power switching method. One possible mechanism is temperature dependence of the leakage current which flows between the gate voltage lead and the pump channel, and contributes to the measured current. This leakage current is the parallel sum of several contributions due to the experimental wiring, sample holder circuit board, and possibly the sample gate oxide itself, and it is likely to be temperature dependent. Temperature changes of the relevant components due to heating from the RF power possibly result in a thermal time constant appearing in the current. This hypothesis is supported by the data of panel (d), in which the time constant appears in the absence of any pump current, with the pump tuned far from the $N = 1$ plateau. However, the total absence of a time constant in the Aalto data of Figure S4(b) remains without a convincing explanation.

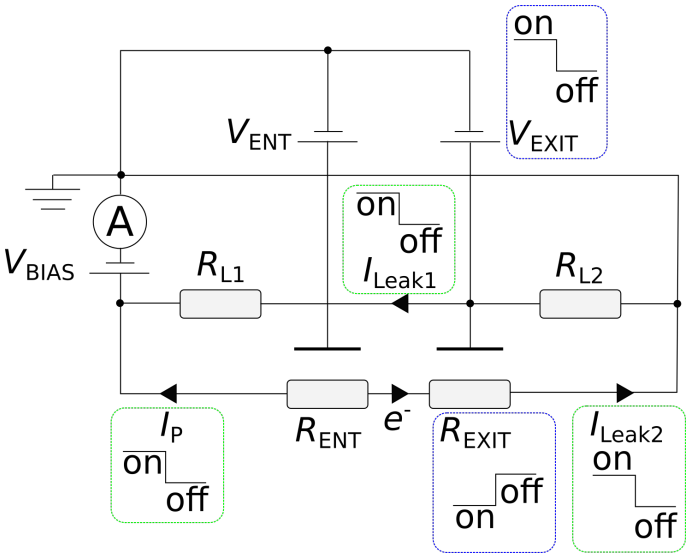

FIG. S5. Schematic circuit diagram illustrating two possible sources of leakage current when the on-off cycle is implemented by stepping the exit gate voltage. The ULCA is depicted as an ammeter in series with a stray bias voltage source V_{BIAS} at the left of the diagram. The potential barriers forming the pump are shown as large resistances R_{ENT} and R_{EXIT}. The meanings of the other circuit elements are explained in the accompanying supplementary text.

E. LEAKAGE CORRECTION

Precision measurements carried out using the gate switching on-off cycle are corrected for leakage currents which, as noted in the previous supplementary section, are driven through nominally insulating parts of the sample, sample holder and experimental wiring. These currents are present all the time in precision measurements, but are assumed constant when the gate voltages are constant. A schematic circuit diagram in figure S5 illustrates two possible sources of leakage current. Here, the sample has been reduced to an electrical circuit consisting of two large resistances in series, R_{ENT} and R_{EXIT}, caused by the potential barriers under the entrance and exit gates. When the pump drive signal is on, the entrance gate voltage is oscillating, but for the purposes of this analysis R_{ENT} can be considered the time-averaged value of the entrance barrier resistance. Electrons are pumped from left to right, and hence the ULCA connected on the source side of the device measures a pump current I_{P} with a positive sign. A leakage current I_{Leak1} is driven by V_{EXIT} through resistance R_{L1}, which is the parallel sum of leakage resistances in the sample, sample holder, and experimental wiring. As an order-of-magnitude estimate, typical isolation between leads in a cryogenic wiring setup is 10^{15} Ω. Thus, a gate voltage of −1 V drives a current of 1 fA, or 6 ppm of I_{P} in our experiment. When V_{EXIT} is stepped to a more negative value for the 'off' part of the cycle, I_{Leak1} becomes more negative. This yields an on-off leakage error current with the same sign as I_{P}: the current evaluated from the on-off cycle is larger than the pump current. Note that leakage current also flows in the resistance R_{L2} to the drain lead of the pump, but as this current does not pass through the ammeter it does not cause an error.

An additional source of leakage current is the stray bias present at the ULCA input, V_{BIAS}. This drives a DC current I_{Leak2} through the pump. The large potential barriers formed by the entrance and exit gates at the pump operation point, combined with the low stray bias of the ULCA make this current very small: for $V_{\mathrm{BIAS}} = 10$ μV and R_{ENT}, $R_{\mathrm{EXIT}} \sim 10^{12}$ Ω, $I_{\mathrm{Leak2}} \sim 10^{-17}$ A, which is less than 0.1 ppm of I_{P}. When V_{EXIT} is switched to a more negative value to turn the pump off, I_{Leak2} decreases. This gives an on-off leakage error current which depends on the sign of V_{BIAS}, and which has the opposite sign to I_{P} for the sign of V_{BIAS} indicated in the diagram.

Measurements made at MIKES and NPL using the gate switching on-off cycle, denoted NPL 2 and MIKES 2 in figure 4 of the main text, are corrected for leakage current: $I_{\mathrm{P}} = \Delta I - \Delta I_{\mathrm{Leak}}$. Here, ΔI is the on-off difference current from the precision pump current measurement with the AC pump drive turned on, and ΔI_{Leak} is the on-off difference current in a leakage measurement with the AC pump drive turned off. Measurements of ΔI_{Leak} at NPL and MIKES gave (91±67) aA and (−162±50) aA respectively. Note the different signs, consistent with the possibility outlined above of two different leakage mechanisms. After correcting for leakage currents, the measurements exploiting the gate switching cycle were consistent with those made using the power switching cycle at both NPL and MIKES, despite the opposite signs for the leakage correction.

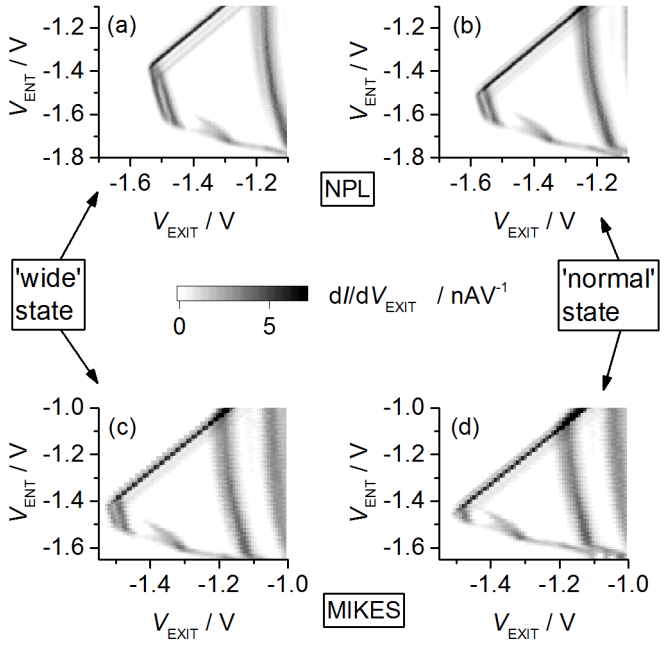

FIG. S6. Pump maps illustrating the 'wide' (panels a and c) and 'normal' (panels b and d) states exhibited by the pump. Panels (a) and (b) were measured at NPL with $P_{RF} = 11.6$ dBm, and panels (c) and (d) were measured at MIKES with $P_{RF} = 12.25$ dBm.

F. BISTABILITY OF PUMP MAP

The pump map was usually stable for several weeks at liquid helium temperatures, but it occasionally switched to a different state characterised by a more extended plateau along the V_{ENT} axis, as well as a transition to the $N = 1$ plateau at slightly more positive V_{EXIT}. We refer to this state as the 'wide' state, to distinguish it from the 'normal' state. Transitions to the wide state did not occur with sufficient regularity to determine a cause, but at NPL they appeared to be correlated with setting the gate voltages to zero. Once in the wide state, the pump switched back to the normal state within 1-2 days. Example pump maps in figure S6 show the normal and the wide states measured at NPL and MIKES. To maintain consistency, all the data presented in this paper was taken with the pump in the normal state.

G. LOW-NOISE CRYOGENIC WIRING

Simply lowering a device into a dewar of liquid helium is a very simple way of cooling it to a temperature of 4 K. However, the dewar presents presents a demanding environment for low-noise current measurements and in this work, the use of the same custom-made cryogenic probe at the three institutes was important for achieving sub-ppm resolution. Bubbles can form in the liquid and cause vibration, while the temperature gradient along the wires can change as the liquid level drops, causing current noise spikes due to triboelectric processes as the wires are subject to changing mechanical strain. Many tests were carried out on different types of wiring to determine the best configuration for low-noise current measurements in a helium dewar. These tests, and their conclusions, will be the subject of a future paper. Here, we summarise the final experimental configuration. The DC experimental wiring consists of 10 enameled constantan wires of approximately 0.4 mm diameter (not all of the wires are used in this experiment). They are stuck together into a flat ribbon, with no twisting, using general electrical varnish. It is important that the ribbon consisted of parallel wires, rather than the commonly-used set of twisted pairs. Twisting the wires introduces strain which can be a source of triboelectric current spikes, and is in any case not as important for current measurement as it is for voltage measurement, where the loop area must be minimised to prevent inductive coupling of interference. The loom is threaded through a 3 mm inside-diameter stainless steel tube which runs from the breakout box at the top of the probe to approximately 5 cm above the sample holder. The purpose of this tube is to contain the wiring loom and prevent it from vibrating within the larger (approximately 1 cm inside-diameter) structural tube of the probe. The 'cold' ends of the wires are terminated with SSMB connectors to mate with the NPL-designed sample holder, and the 'warm' ends terminate inside the breakout box which has BNC connections. The room-temperature cable from the probe breakout box to the ULCA input is the specialised low-noise cable supplied with the ULCA. A final important detail on the cryogenic probe construction is that the use of insulating tape is kept to a minimum throughout the probe, as insulating tape can carry charge which will generate a current in a wire nearby if that wire vibrates.

[1] D. Drung, C. Krause, U. Becker, H. Scherer, and F. J. Ahlers, "Ultrastable low-noise current amplifier: A novel device for measuring small electric currents with high accuracy," Review of Scientific Instruments **86**, 024703 (2015).
[2] R. Zhao, A. Rossi, S. Giblin, J. Fletcher, F. Hudson, M. Möttönen, M. Kataoka, and A. Dzurak, "Thermal-error regime in high-accuracy gigahertz single-electron pumping," Physical Review Applied **8**, 044021 (2017).
[3] F. Stein, H. Scherer, T. Gerster, R. Behr, M. Götz, E. Pesel, C. Leicht, N. Ubbelohde, T. Weimann, K. Pierz, *et al.*, "Robustness of single-electron pumps at sub-ppm current accuracy level," Metrologia **54**, S1 (2017).
[4] C. Krause, D. Drung, M. Götz, and H. Scherer, "Noise-optimized ultrastable low-noise current amplifier," Review of Scientific Instruments **90**, 014706 (2019).
[5] F. Stein, D. Drung, L. Fricke, H. Scherer, F. Hohls, C. Leicht, M. Goetz, C. Krause, R. Behr, E. Pesel, U. Siegner, F.-J. Ahlers, and H. W. Schumacher, "validation of a quantized-current source with 0.2 ppm uncertainty," Applied Physics Letters **107**, 103501 (2015).
[6] G. Yamahata, S. P. Giblin, M. Kataoka, T. Karasawa, and A. Fujiwara, "Gigahertz single-electron pumping in silicon with an accuracy better than 9.2 parts in 10^7," Applied Physics Letters **109**, 013101 (2016).

[7]S. Giblin, M. Bae, N. Kim, Y.-H. Ahn, and M. Kataoka, "Robust operation of a gallium arsenide tunable barrier electron pump," Metrologia **54**, 299 (2017).
[8]S. P. Giblin, M. Kataoka, J. D. Fletcher, P. See, T. Janssen, J. P. Griffiths, G. A. C. Jones, I. Farrer, and D. A. Ritchie, "Towards a quantum representation of the ampere using single electron pumps," Nature Communications **3**, 930 (2012).
[9]M.-H. Bae, Y.-H. Ahn, M. Seo, Y. Chung, J. D. Fletcher, S. P. Giblin, M. Kataoka, and N. Kim, "Precision measurement of a potential-profile tunable single-electron pump," Metrologia **52**, 195 (2015).